CMS Physics Analysis Summary

Contact: cms-pag-conveners-smp@cern.ch 2013/05/16

Measurement of the double-differential inclusive jet cross section at $\sqrt{s} = 8\,\text{TeV}$ with the CMS detector

The CMS Collaboration

Abstract

A measurement of the inclusive jet cross section, double-differential in jet transverse momentum p_T and absolute jet rapidity $|y|$, is presented. Data from LHC proton-proton collisions at $\sqrt{s} = 8\,\text{TeV}$, corresponding to an integrated luminosity of $10.71\,\text{fb}^{-1}$, have been collected with the CMS detector. Jets are reconstructed with the anti-k_T clustering algorithm for a jet size parameter $R = 0.7$ in a phase space region ranging up to jet transverse momenta of $p_\text{T} = 2.5\,\text{TeV}$ and an absolute rapidity of $|y| = 3.0$. The measured jet cross section is corrected for detector effects and compared to predictions of perturbative QCD at next-to-leading order using various sets of parton distribution functions.

1 Introduction

Proton-proton collisions leading to events with high transverse momentum jets are described by quantum chromodynamics (QCD) through parton-parton scattering. A fundamental quantity that can be measured and predicted within the framework of perturbative QCD (pQCD) is the inclusive jet cross section (p + p $\rightarrow$ jet + X), where every jet is counted. In the presented analysis this is performed double-differentially as a function of the jet transverse momentum p_{T} and the absolute jet rapidity $|y|$. In detailed studies the data reported here can be used to constrain the parton distribution functions (PDFs) of the proton or to determine the strong coupling constant α_S. Previous measurements have been carried out at the LHC by the ATLAS and CMS collaborations at 7 TeV centre-of-mass energy [1–4] as well as by experiments at other hadron colliders [5–9].

The data were collected with the Compact Muon Solenoid (CMS) detector at the CERN Large Hadron Collider (LHC) during the 2012 run and correspond to an integrated luminosity of 10.71 fb^{-1}. The measured cross sections are corrected for detector effects and compared to the QCD predictions. The momentum fraction, x, of the proton carried by the partons participating in the hard interaction, probed in this measurement cover the range $0.019 < x < 0.625$.

2 Apparatus

The central feature of the CMS apparatus is a superconducting solenoid of 6 m internal diameter, providing a magnetic field of 3.8 T. Within the superconducting solenoid volume are a silicon pixel and strip tracker, a lead tungstate crystal electromagnetic calorimeter (ECAL), and a brass/scintillator hadron calorimeter (HCAL). Muons are measured in gas-ionization detectors embedded in the steel return yoke outside the solenoid. Extensive forward calorimetry complements the coverage provided by the barrel and endcap detectors.

CMS uses a right-handed coordinate system, with the origin at the nominal interaction point, the x axis pointing to the centre of the LHC, the y axis pointing up (perpendicular to the LHC plane), and the z axis along the anticlockwise-beam direction. The polar angle θ is measured from the positive z axis and the azimuthal angle ϕ is measured in the x-y plane. The pseudorapidity and rapidity are then defined as $\eta = -\ln[\tan(\theta/2)]$ and $y = \frac{1}{2}\ln[(E + p_z)/(E - p_z)]$, where E is the energy and p_z is the momentum component along the z axis. The transverse momentum p_{T} is calculated from p_x and p_y, the momentum components along the x and y axes, as $p_{\mathrm{T}} = \sqrt{p_x^2 + p_y^2}$.

In the region $|\eta| < 1.74$, the HCAL cells have widths of 0.087 in pseudorapidity and 0.087 in azimuth (ϕ). In the η-ϕ plane, and for $|\eta| < 1.48$, the HCAL cells map on to 5×5 ECAL crystals arrays to form calorimeter towers projecting radially outwards from close to the nominal interaction point. At larger values of $|\eta|$, the size of the towers increases and the matching ECAL arrays contain fewer crystals. Within each tower, the energy deposits in ECAL and HCAL cells are summed to define the calorimeter tower energies, subsequently used to provide the energies and directions of hadronic jets.

The energy resolution for photons with $E_{\mathrm{T}} \approx 60$ GeV varies between 1.1% and 2.5% over the solid angle of the ECAL barrel, and from 2.2% to 5% in the endcaps. The HCAL, when combined with the ECAL, measures jets with a resolution $\Delta E/E \approx 100\%/\sqrt{E\,[\mathrm{GeV}]} \oplus 5\%$. A more detailed description of the CMS detector can be found in Ref. [10].

3 Jet reconstruction

In the CMS experiment, the particle-flow event reconstruction [11] is employed, which consists in reconstructing and identifying each single particle with an optimized combination of all subdetector information. The energy of photons is directly obtained from the ECAL measurement, corrected for zero-suppression effects. The energy of electrons is determined from a combination of the track momentum at the main interaction vertex, the corresponding ECAL cluster energy, and the energy sum of all bremsstrahlung photons attached to the track. The energy of muons is obtained from the corresponding track momentum. The energy of charged hadrons is determined from a combination of the track momentum and the corresponding ECAL and HCAL energy, corrected for zero-suppression effects, and calibrated for the nonlinear response of the calorimeters. Finally the energy of neutral hadrons is obtained from the corresponding calibrated ECAL and HCAL energy.

The jet clustering is performed on the four momenta of the reconstructed particle candidates with the anti-k_T jet algorithm [12] for a jet size parameter of $R = 0.7$ using the FASTJET package [13]. The jet momentum is determined as the vectorial sum of all particle momenta in the jet, and is found in the simulation to be within 5% to 10% of the true momentum over the whole p_T spectrum and detector acceptance. An offset correction is applied to take into account the extra energy clustered into jets due to additional proton-proton interactions within the same or neighboring bunch crossings (pile-up) [14]. Jet energy corrections are derived from the simulation, and are confirmed with in situ measurements with the energy balance of dijet, photon+jet and Z+jet events [14]. Additional selection criteria are applied to each event to remove spurious jet-like features originating from isolated noise patterns in certain HCAL regions.

The jet-energy correction depends on the η and p_T of each jet, and is applied as a multiplicative factor to the jet four-momentum vector. The multiplicative factor is in general smaller than 1.2. For a jet with a p_T of 100 GeV the typical factor is 1.1, decreasing towards 1.0 with increasing p_T. The jet energy resolution amounts typically to 8% at 100 GeV and 4% at 1 TeV.

4 Event selection

The CMS detector records events using a two-level trigger system consisting of a hardware-based level-1 (L1) trigger [15] and a software-based high level trigger (HLT) [16]. In this study, single-jet triggers that reconstruct jets from calorimeter energy deposits at L1 and from particle-flow jets at HLT are used to select events. The data samples are collected with six single-jet HLT which require at least one jet in the event with corrected jet $p_T > 40$, 80, 140, 200, 260, and 320 GeV, respectively. All except the highest-threshold trigger were prescaled during the 2012 run. The efficiency of each of the triggers is estimated using lower-p_T-threshold triggers to ensure more than 99% trigger efficiency. The prescale factors along with the corresponding effective integrated luminosity $\mathcal{L}_{\text{int,eff}}$ and the p_T thresholds of each trigger path are shown in Table 1 for the different running periods.

In the offline analysis events are required to have at least one reconstructed vertex [17] along the beam line that is within 24 cm of the nominal interaction point. To suppress nonphysical jets, i.e. jets resulting from noise in the ECAL and/or HCAL calorimeters, tight identification criteria are applied [18]: each jet should contain at least two particles, one of which is a charged hadron, and the jet energy fraction carried by neutral hadrons, photons, muons, and electrons should be less than 90%. These criteria have an efficiency greater than 99% for genuine jets. Jets not satisfying the tight identification requirements are discarded. Events are selected if at least one jet remains above the threshold of the highest p_T threshold trigger that recorded the event.

Table 1: HLT trigger thresholds, prescale factors and effective integrated luminosities for each running period.

HLT Path		PFJet40	PFJet80	PFJet140	PFJet200	PFJet260	PFJet320
p_T range (GeV)		74 - 133	133 - 220	220 - 300	300 - 395	395 - 507	507 - 2500
Running period	Prescale	60000	3000	230	80	10	1
2012A	$\mathcal{L}_{\text{int,eff}}$ (pb^{-1})	0.010	0.195	2.782	14.08	60.57	611.02
Running period	Prescale	250000	7000	270	70	15	1
2012B	$\mathcal{L}_{\text{int,eff}}$ (pb^{-1})	0.017	0.630	16.30	64.08	266.286	4140
Running period	Prescale	220500	10000	400	80	20	1
2012C	$\mathcal{L}_{\text{int,eff}}$ (pb^{-1})	0.020	0.533	15.767	79.292	317.158	5966
Total	$\mathcal{L}_{\text{int,eff}}$ (pb^{-1})	0.047	1.358	34.85	157.45	644.014	10717.02

5 The measurement

The double-differential inclusive jet cross section is defined as

$$\frac{\mathrm{d}^2\sigma}{\mathrm{d}p_T \mathrm{d}y} = \frac{1}{\epsilon \mathcal{L}_{\text{int,eff}}} \frac{N_{\text{jets}}}{\Delta p_T \, \Delta y}, \tag{1}$$

where N_{jets} is the number of jets in a bin, ϵ is the product of the trigger and jet selection efficiencies (greater than 99%), and Δp_T and Δy are the transverse momentum and rapidity bin widths, respectively. The width of the p_T bins increases progressively with p_T, proportional to the p_T resolution. The phase space in rapidity y is subdivided into six equally sized regions of absolute rapidity from $|y| = 0.0$ up to $|y| = 3.0$ with $\Delta|y| = 0.5$. Hence, the bin width in y is $\Delta y = 1.0$.

The statistical uncertainty for each bin is corrected for the effect that multiple jet entries per event may arise [4]. This correction is small, since in the entire phase-space considered here at least 90% of the observed jets in each bin originate from different events.

To account for residual effects of small inefficiencies from triggering or jet identification a conservative uncertainty of 1% uncorrelated across all jet p_T and y bins is assigned to each bin.

In Eq. 1 $\mathcal{L}_{\text{int,eff}}$ is the effective integrated luminosity of a bin, taking into account the corresponding trigger prescale factors, from which the events are taken, as given in Table 1. The measured spectra are then unfolded for detector effects using the iterative Bayesian method [19, 20] as implemented in the RooUnfold package [21]. The response matrix is created by smearing the theoretically predicted spectrum as presented in Section 6. The theoretical p_T spectrum is fitted with a falling function. The response matrices, describing the mapping between the particle jets spectra and reconstructed jets spectra, are constructed extracting the particle level jet spectrum from this fitted function and the reco level jet spectrum, which is obtained by smearing the particle level jet spectrum with the jet energy resolution (JER) parameters.

The JER is taken from Monte Carlo (MC) simulation and is corrected by factors derived from data [14]. It is parametrized as a function of jet p_T as:

$$\frac{\sigma(p_T)}{p_T} = \sqrt{\frac{N^2}{p_T^2} + \frac{S^2}{p_T} + C^2}, \tag{2}$$

where the fitted parameters N, S, and C are listed in Table 2.

Table 2: The fitted parameters of the jet energy resolution formula 2 for each rapidity region.

$\|y\|$ bin	0.0–0.5	0.5–1.0	1.0–1.5	1.5–2.0	2.0–2.5	2.5–3.0
N	0.032	0.038	0.043	0.017	0.016	0.022
S	1.136	1.053	1.112	1.034	0.878	0.945
C	5.886	6.577	6.743	8.147	8.334	7.534

Through the unfolding procedure the final statistical uncertainties become correlated between the unfolded bins. The size of these correlations vary typically between 10 to 20%.

In the Bayesian unfolding process [21], the number of estimated events in the i-th bin of the unfolded distribution ('estimated causes') $\hat{n}(C_i)$, as the result of applying the unfolding matrix M_{ij} on the j-th bin of raw distribution ('effects'), containing $n(E_j)$ events, is given by:

$$\hat{n}(C_i) = \sum_{j=1}^{n_E} M_{ij} n(E_j)$$

where

$$M_{ij} = \frac{P(E_j|C_i) n_0(C_i)}{\epsilon_i \sum_{l=1}^{n_C} P(E_j|C_l) n_0(C_l)}.$$

Here $P(E_j|C_i)$ is the $n_E \times n_C$ response matrix, where n_E and n_C are the number of bins in raw and unfolded distributions respectively. This response matrix causes correlation among different bins in the unfolded distribution. Here $\epsilon_i = \sum_{j=1}^{n_E} P(E_j|C_i)$ are efficiencies for each bin and $n_0(C_l)$ is the number of entries in the l-th bin of the prior distribution. Output of each iteration of unfolding goes as prior distribution to the next iteration.

The experimental systematic uncertainty on the measured cross section is dominated by the uncertainty on the jet-energy scale, which is composed of twenty independent sources [14]. The JES uncertainty varies between 2 to 5% in the different p_{T} bins and is almost uniform across the rapidity bins. The total experimental uncertainty consists of unfolding , JES and luminosity uncertainty. It induces an uncertainty of 15 to 30% on the inclusive jet cross section at central rapidity, which increases to 15 to 40% in the outer rapidity region.

The unfolding uncertainty is derived from simulation. The jet-energy resolution (JER) is determined from MC. The fitted JER parameters are then varied by 10% up and down to determine how much it affects the unfolded spectrum. The jet-energy resolution uncertainty of 10% [14] affects the unfolding, and introduces a 1-10% uncertainty on the cross section. To estimate the uncertainty introduced due to parametrization of the fitting function, used to fit the spectrum, the fitted parameters are varied by $\pm 5\%$ and the response matrices were produced to unfold the measured spectrum. The final unfolded spectrum has negligible effect due to this variation of parametrization. The total unfolding uncertainty includes the JER uncertainty. The uncertainty on the integrated luminosity is 4.4% [22] and propagates directly to the cross section. Other sources of uncertainties, such as the jet angular resolution and the theoretical p_{T} spectrum used to calculate the response matrix, introduce negligible change on the cross section.

6 Theory predictions

The theoretical predictions for the jet cross sections are derived at next-to-leading order accuracy (NLO) in perturbative QCD. The NLO calculations are performed using the NLOJET++ program version 4.1.3 [23, 24] within the framework of the FASTNLO package version 2.1 [25]. The renormalization (μ_R) and factorization scale (μ_F) are identified with the jet p_{T}. The calculations are performed using the following five sets of parton distribution functions: CT10 [26], MSTW2008 [27], NNPDF2.1 [28], HERAPDF1.5 [29], and ABM11 [30], each at NLO evolution order and with the corresponding default value of the strong coupling constant of 0.1180, 0.1202, 0.1190, 0.1176, and 0.1180, respectively.

In order to account for effects of multi-parton interactions (MPI) and hadronization, a nonperturbative correction factor (NP) is applied to the NLO prediction. The NP effects are estimated from simulation using the event generators PYTHIA6 [31] tune Z2star and HERWIG++ version 2.4.2 [32] tune UE. These two MC event generators are representative of different physics models for the NP corrections. The NP correction factor is defined as

$$C_{\mathrm{NP}} = \sigma(\mathrm{Nominal})/\sigma(\mathrm{noMPI,noHAD})\,, \tag{3}$$

where *Nominal* means the default settings of the corresponding tune, while *noMPI,noHAD* refers to a steering parameter set with MPI and hadronization switched off. The size of the corrections ranges from 20% at low p_{T} down to 1% at highest p_{T} of 2.5 TeV.

The uncertainty of the NLO pQCD calculation is estimated following the conventional recipe of varying the renormalization and factorization scale by the following six combinations of scale factors:
$(\mu_F/\mu, \mu_R/\mu) = (0.5, 0.5)$, $(2, 2)$, $(1, 0.5)$, $(1, 2)$, $(0.5, 1)$, $(2, 1)$, where $\mu =$ jet p_{T}. The scale uncertainty then ranges from 5% to 10% for $|y| < 1.5$ and increases to 40% for the outer $|y|$ bins and for high jet p_T.

The prescriptions to evaluate PDF uncertainties lead to a 5 to 30% uncertainty on the predicted cross section in the entire p_{T} range for $|y| \leq 1.5$. Beyond $|y| = 1.5$ in the outer rapidity region the uncertainties become as large as 50% at high p_{T} and even increase up to 100% for the CT10 and HERAPDF1.5 sets.

The NP correction induces an additional uncertainty, which is estimated to reach at most 10% at low jet p_{T} s around 100 GeV, decreasing to less than 1% at high p_{T}. Overall, the PDF uncertainty is dominant.

7 Comparison of theory and data

Figure 1 shows the inclusive jet cross section, unfolded for detector effects and double-differentially in jet p_{T} and y, in comparison to the theory prediction at NLO with the NNPDF2.1 PDF set times the NP correction factor. At a logarithmic scale the data are well described by the prediction of QCD over many orders of magnitude in cross section and for jet p_{T} s ranging from 74 GeV up to 2.5 TeV.

In order to reveal finer details, the ratio of the data to the NLO prediction times the NP correction factor is shown for the five investigated PDF sets in Figs. 2–6. In addition, the total experimental systematic and total theoretical uncertainties are shown as bands around one. It is remarkable that in most cases the theory predictions agree with the data within uncertainties.

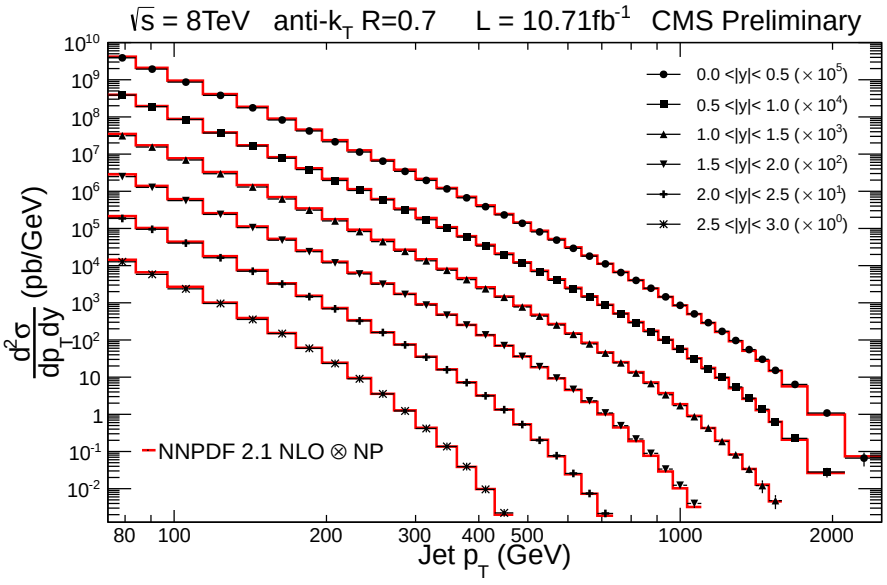

Figure 1: Double-differential inclusive jet cross section in comparison to NLO predictions using the NNPDF2.1 PDF set times the NP correction factor.

The only exception occurs when comparing to the ABM11 PDF set in Fig. 5, where significant discrepancies are visible.

In Figures 7–11 a similar comparison is performed, but instead of the theoretical uncertainty for each PDF set the ratios of the predictions with alternative PDF sets are shown. This better allows to judge the (dis-)agreement between the various PDF sets. As with the previous comparison most predictions are rather similar except for the ABM11 PDF set that exhibits a significantly different behaviour. Final quantitative conclusions on the agreement between the predictions employing the various PDF sets and the data is left to a more detailed study that must include correlated uncertainties.

8 Summary

A measurement of the inclusive jet cross section is presented using 10.71 fb^{-1} of data from proton-proton collisions at $\sqrt{s} = 8$ TeV collected with the CMS detector. The result is presented double-differentially as a function of jet transverse momentum p_{T} and rapidity y and covers a large range in jet p_{T} from 74 GeV up to 2.5 TeV, in six rapidity bins up to $|y| = 3.0$. The parton momentum fractions x probed in this measurement cover the range $0.019 < x < 0.625$.

Detailed studies of experimental and theoretical sources of uncertainty have been carried out. The dominant source of experimental systematic uncertainty arises due to the jet energy scale, unfolding and luminosity measurement uncertainty. These leads to about 15-40% uncertainty in the cross section measurement across various rapidity bins. In comparison, the theory predictions are most affected by PDF uncertainties, which amount to 10% to 50% depending on the rapidity bin, whereas choices of renormalization and factorization scales contribute 5% to 10% at central rapidity and 40% in the outer rapidity bins.

In a qualitative comparison it is demonstrated that perturbative QCD (times a small nonperturbative correction) is able to well describe the data over a wide range of jet transverse momentum and rapidity and over many orders of magnitude in cross section. In detail, some differences between the predictions employing various PDF sets and to the data are observed,

all of which are qualitatively covered by uncertainties except for the ABM11 PDF set, which exhibits significant deviations.

This new inclusive jet cross section measurement probes a wide range in x and momentum scale Q and hence can be used to constrain PDFs and to determine the strong coupling constant in a new kinematic regime.

References

[1] ATLAS Collaboration, "Measurement of inclusive jet and dijet cross sections in proton-proton collisions at 7 TeV centre-of-mass energy with the ATLAS detector", *Eur. Phys. J. C* **71** (2011) 1512, doi:10.1140/epjc/s10052-010-1512-2, arXiv:1009.5908.

[2] CMS Collaboration, "Measurement of the Inclusive Jet Cross Section in pp Collisions at 7 TeV", *Phys. Rev. Lett.* **107** (2011) 132001, doi:10.1103/PhysRevLett.107.132001.

[3] ATLAS Collaboration, "Measurement of inclusive jet and dijet production in pp collisions at $\sqrt{s} = 7$ TeV using the ATLAS detector", *Phys. Rev. D* **86** (2012) 014022, doi:10.1103/PhysRevD.86.014022, arXiv:1112.6297.

[4] CMS Collaboration, "Measurements of differential jet cross sections in proton-proton collisions at $\sqrt{s} = 7$ TeV with the CMS detector", technical report, (2012).

[5] UA2 Collaboration, "Observation of Very Large Transverse Momentum Jets at the CERN $\bar{p}p$ Collider", *Phys. Lett. B* **118** (1982) 203, doi:10.1016/0370-2693(82)90629-3.

[6] UA1 Collaboration, "Hadronic Jet Production at the CERN Proton-Antiproton Collider", *Phys. Lett. B* **132** (1983) 214, doi:10.1016/0370-2693(83)90254-X.

[7] CDF Collaboration, "Measurement of the Inclusive Jet Cross Section using the k_{T} algorithm in $p\bar{p}$ Collisions at $\sqrt{s}$ = 1.96 TeV with the CDF II Detector", *Phys. Rev. D* **75** (2007) 092006, doi:10.1103/PhysRevD.75.119901,10.1103/PhysRevD.75.092006, arXiv:hep-ex/0701051.

[8] D0 Collaboration, "Measurement of the inclusive jet cross-section in $p\bar{p}$ collisions at $\sqrt{s}$ = 1.96 TeV", *Phys. Rev. Lett.* **101** (2008) 062001, doi:10.1103/PhysRevLett.101.062001, arXiv:0802.2400.

[9] CDF Collaboration, "Measurement of the Inclusive Jet Cross Section at the Fermilab Tevatron $p\bar{p}$ Collider Using a Cone-Based Jet Algorithm", *Phys. Rev. D* **78** (2008) 052006, doi:10.1103/PhysRevD.79.119902,10.1103/PhysRevD.78.052006, arXiv:0807.2204.

[10] CMS Collaboration, "The CMS experiment at the CERN LHC", *JINST* **3** (2008) S08004, doi:10.1088/1748-0221/3/08/S08004.

[11] CMS Collaboration, "Particle–Flow Event Reconstruction in CMS and Performance for Jets, Taus, and MET", *CMS Physics Analysis Summary* **CMS-PAS-PFT-09-001** (2009).

[12] M. Cacciari, G. P. Salam, and G. Soyez, "The anti-k_t jet clustering algorithm", *JHEP* **04** (2008) 063, doi:10.1088/1126-6708/2008/04/063, arXiv:0802.1189.

[13] M. Cacciari, G. P. Salam, and G. Soyez, "FastJet User Manual", *Eur. Phys. J. C* **72** (2012) 1896, doi:10.1140/epjc/s10052-012-1896-2, arXiv:1111.6097.

[14] CMS Collaboration, "Determination of Jet Energy Calibration and Transverse Momentum Resolution in CMS", *JINST* **6** (2011) P11002, doi:10.1088/1748-0221/6/11/P11002.

[15] CMS Collaboration, "Performance of the CMS Level-1 trigger during commissioning with cosmic ray muons and LHC beams", *JINST* **5** (2010) T03002.

[16] CMS Collaboration, "The CMS High Level Trigger", *Eur. Phys. J. C* **46** (2006) 605, doi:10.1140/epjc/s2006-02495-8.

[17] CMS Collaboration, "Tracking and Primary Vertex Results in First 7 TeV Collisions", CMS Physics Analysis Summary CMS-PAS-TRK-10-005, (2010).

[18] CMS Collaboration, "Calorimeter Jet Quality Criteria for the First CMS Collision Data",.

[19] G. D'Agostini, "A Multidimensional unfolding method based on Bayes' theorem", *Nucl. Instrum. Meth. A* **362** (1995) 487, doi:10.1016/0168-9002(95)00274-X.

[20] G. D'Agostini, "Improved iterative Bayesian unfolding", arXiv:physics/1010.0632.

[21] T. Adye, "Unfolding algorithms and tests using RooUnfold", arXiv:1105.1160.

[22] CMS Collaboration, "CMS Luminosity Based on Pixel Cluster Counting - Summer 2012 Update", Technical Report CMS-PAS-LUM-12-001, CERN, Geneva, (2012).

[23] Z. Nagy, "Three jet cross-sections in hadron hadron collisions at next-to-leading order", *Phys. Rev. Lett.* **88** (2002) 122003, doi:10.1103/PhysRevLett.88.122003, arXiv:hep-ph/0110315.

[24] Z. Nagy, "Next-to-leading order calculation of three jet observables in hadron-hadron collision", *Phys. Rev. D* **68** (2003) 094002, doi:10.1103/PhysRevD.68.094002, arXiv:hep-ph/0307268.

[25] D. Britzger et al., "New features in version 2 of the fastNLO project", doi:10.3204/DESY-PROC-2012-02/165, arXiv:1208.3641.

[26] H.-L. Lai et al., "New parton distributions for collider physics", *Phys. Rev. D* **82** (2010) 074024, doi:10.1103/PhysRevD.82.074024.

[27] A. D. Martin et al., "Parton distributions for the LHC", *Eur. Phys. J. C* **63** (2009) 189, doi:10.1140/epjc/s10052-009-1072-5.

[28] R. D. Ball et al., "A first unbiased global NLO determination of parton distributions and their uncertainties", *Nucl. Phys. B* **838** (2010) 136, doi:10.1016/j.nuclphysb.2010.05.008.

[29] H1 and ZEUS Collaboration, "Combined Measurement and QCD Analysis of the Inclusive ep Scattering Cross Sections at HERA", *JHEP* **01** (2010) 109, doi:10.1007/JHEP01(2010)109.

[30] S. Alekhin, J. Blümlein, and S. Moch, "Parton Distribution Functions and Benchmark Cross Sections at NNLO", *Phys. Rev. D* **86** (2012) 054009, doi:10.1103/PhysRevD.86.054009, arXiv:1202.2281.

[31] T. Sjöstrand, S. Mrenna, and P. Skands, "PYTHIA 6.4 physics and manual", *JHEP* **05** (2006) 026, doi:10.1088/1126-6708/2006/05/026.

[32] M. Bähr et al., "Herwig++ Physics and Manual", *Eur. Phys. J. C* **58** (2008) 639, doi:10.1140/epjc/s10052-008-0798-9.

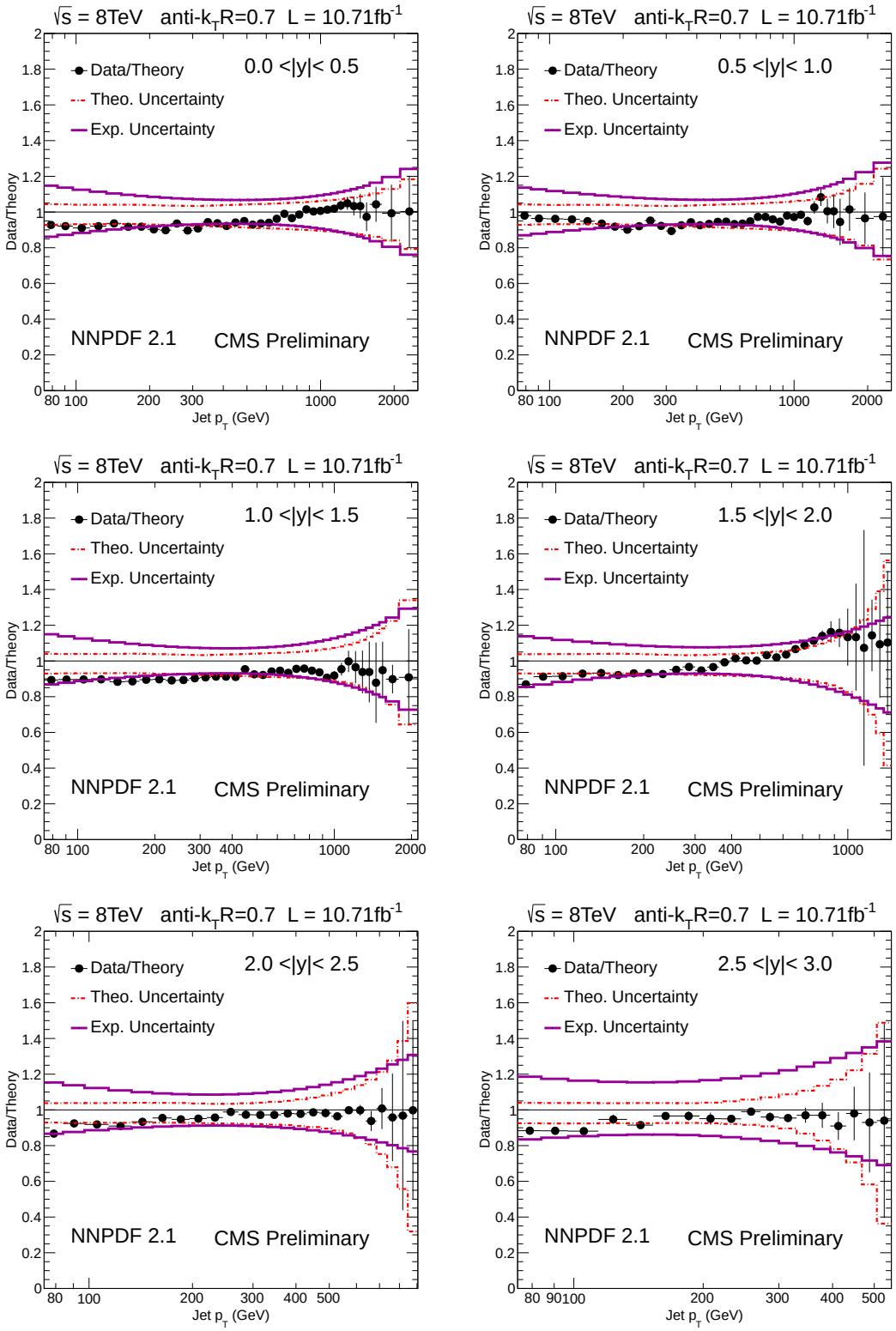

Figure 2: Ratio of data over theory at NLO times NP correction for the NNPDF2.1 PDF set. For comparison the total theoretical (band enclosed by dashed red lines) and the total experimental systematic uncertainty (band enclosed by full magenta lines) are shown as well. The error bars correspond to the statistical uncertainty of the data.

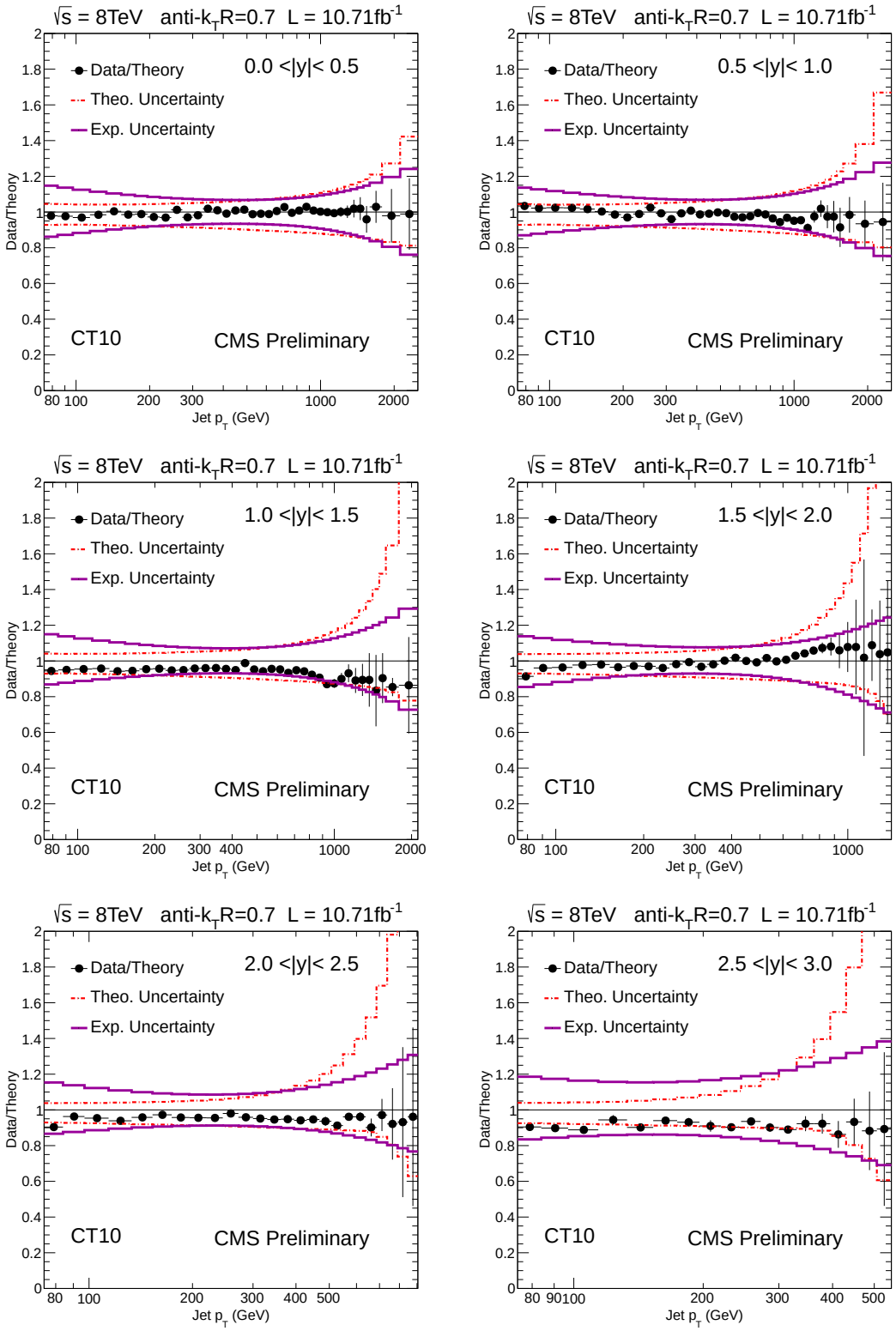

Figure 3: Ratio of data over theory at NLO times NP correction for the CT10 PDF set. For comparison the total theoretical (band enclosed by dashed red lines) and the total experimental systematic uncertainty (band enclosed by full magenta lines) are shown as well. The error bars correspond to the statistical uncertainty of the data.

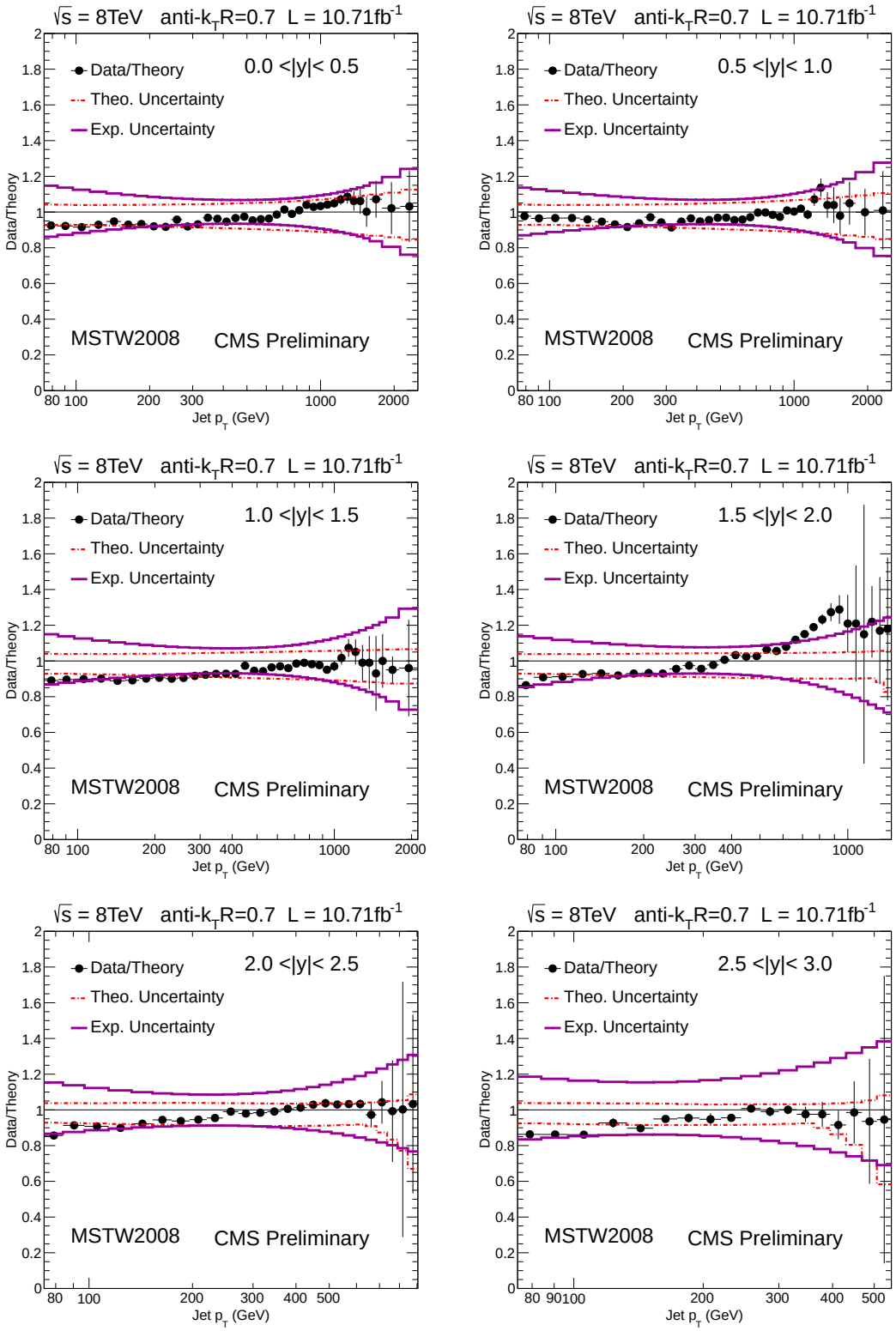

Figure 4: Ratio of data over theory at NLO times NP correction for the MSTW2008 PDF set. For comparison the total theoretical (band enclosed by dashed red lines) and the total experimental systematic uncertainty (band enclosed by full magenta lines) are shown as well. The error bars correspond to the statistical uncertainty of the data.

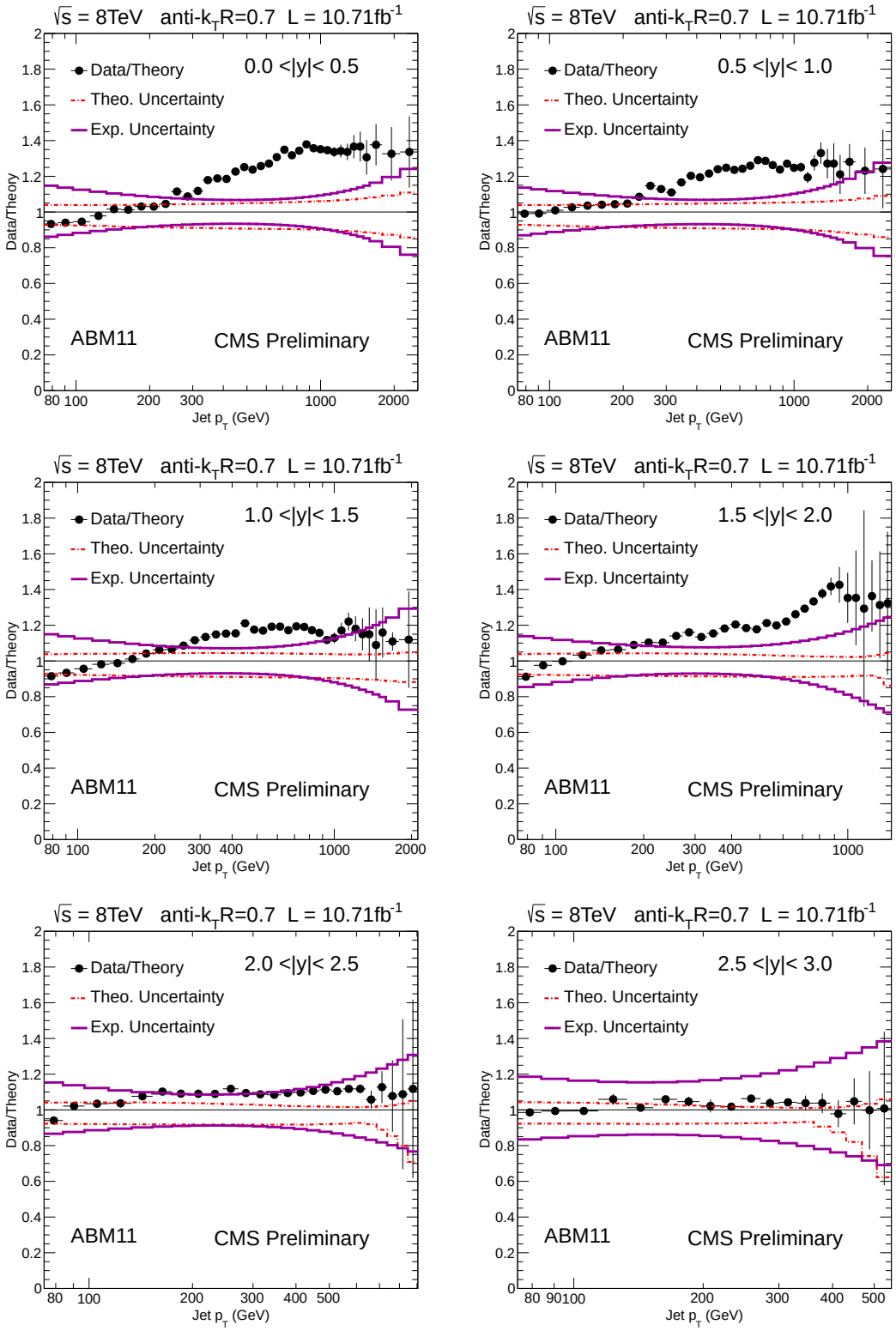

Figure 5: Ratio of data over theory at NLO times NP correction for the ABM11 PDF set. For comparison the total theoretical (band enclosed by dashed red lines) and the total experimental systematic uncertainty (band enclosed by full magenta lines) are shown as well. The error bars correspond to the statistical uncertainty of the data.

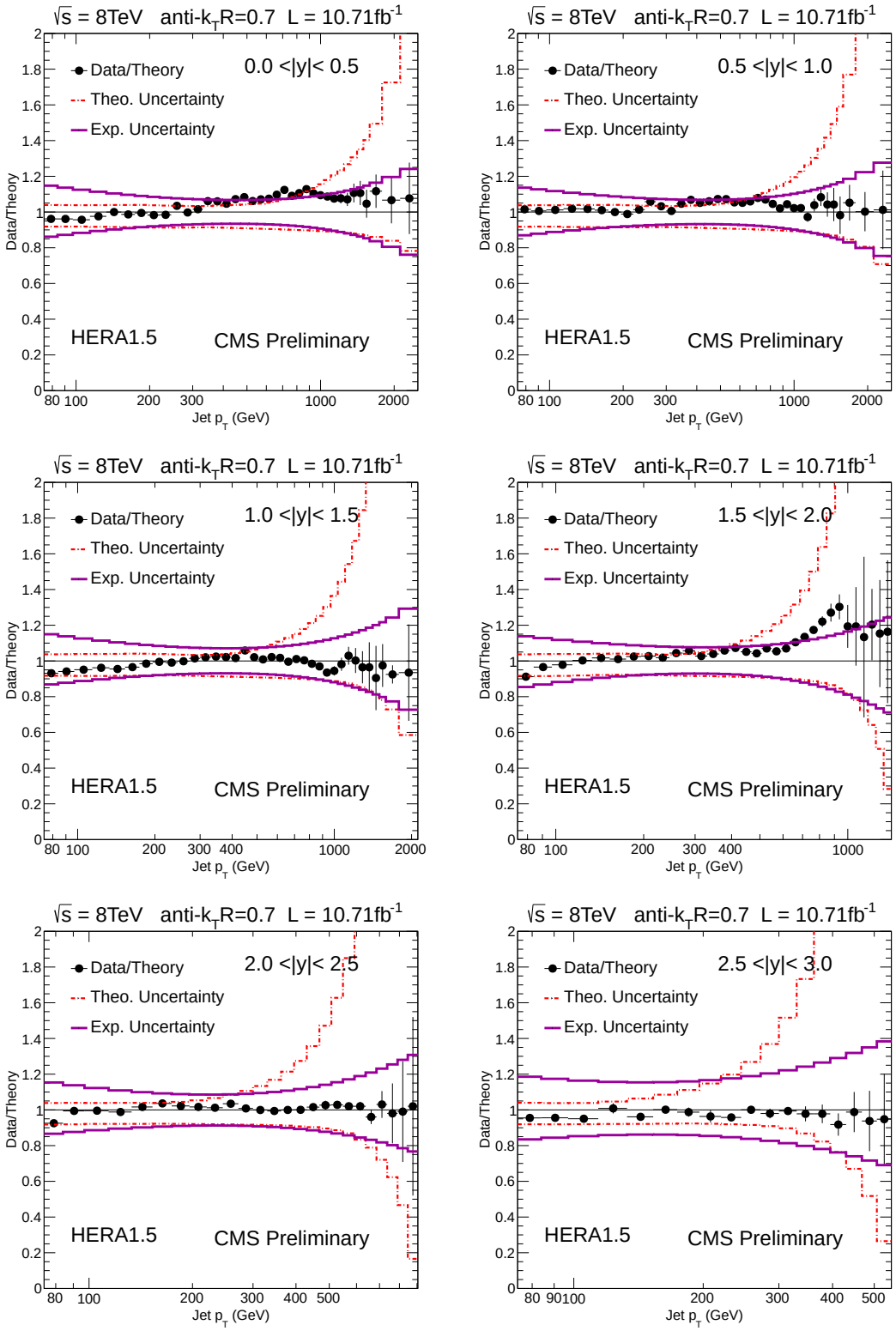

Figure 6: Ratio of data over theory at NLO times NP correction for the HERA1.5 PDF set. For comparison the total theoretical (band enclosed by dashed red lines) and the total experimental systematic uncertainty (band enclosed by full magenta lines) are shown as well. The error bars correspond to the statistical uncertainty of the data.

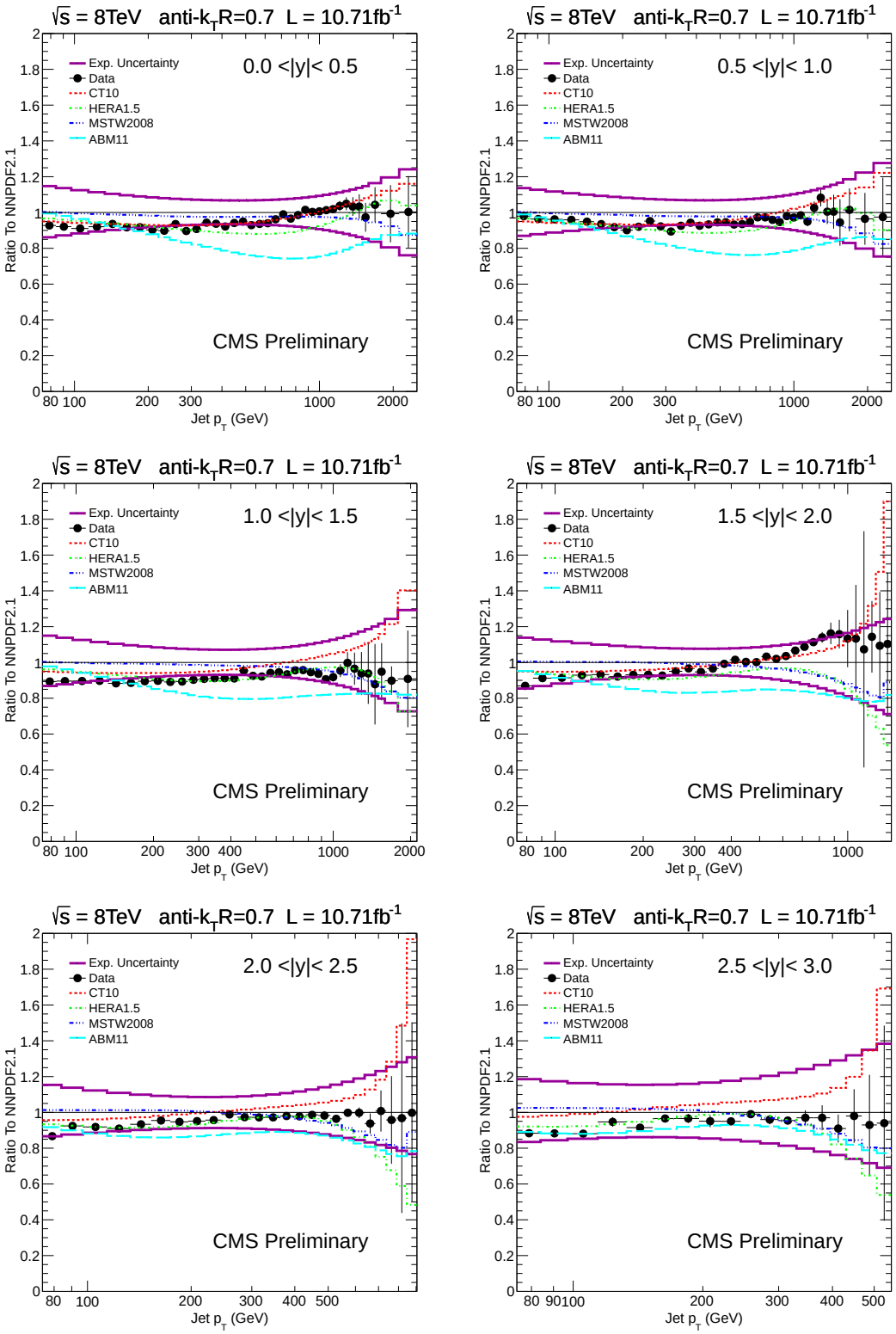

Figure 7: Ratio of data over theory at NLO times NP correction for the NNPDF2.1 PDF set. For comparison predictions employing four other PDF sets are shown in addition to the total experimental systematic uncertainty (band enclosed by full magenta lines). The error bars correspond to the statistical uncertainty of the data.

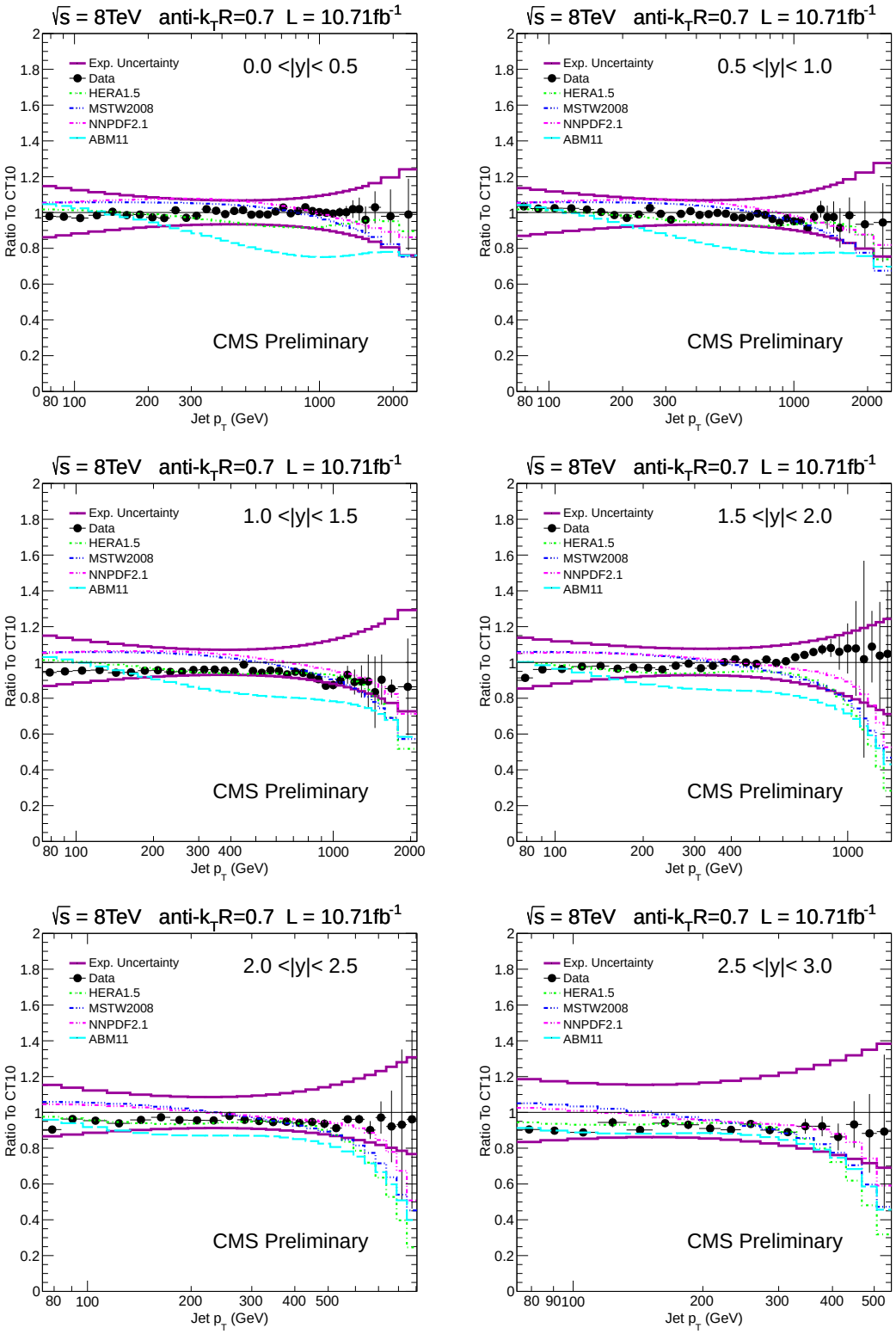

Figure 8: Ratio of data over theory at NLO times NP correction for the CT10 PDF set. For comparison predictions employing four other PDF sets are shown in addition to the total experimental systematic uncertainty (band enclosed by full magenta lines). The error bars correspond to the statistical uncertainty of the data.

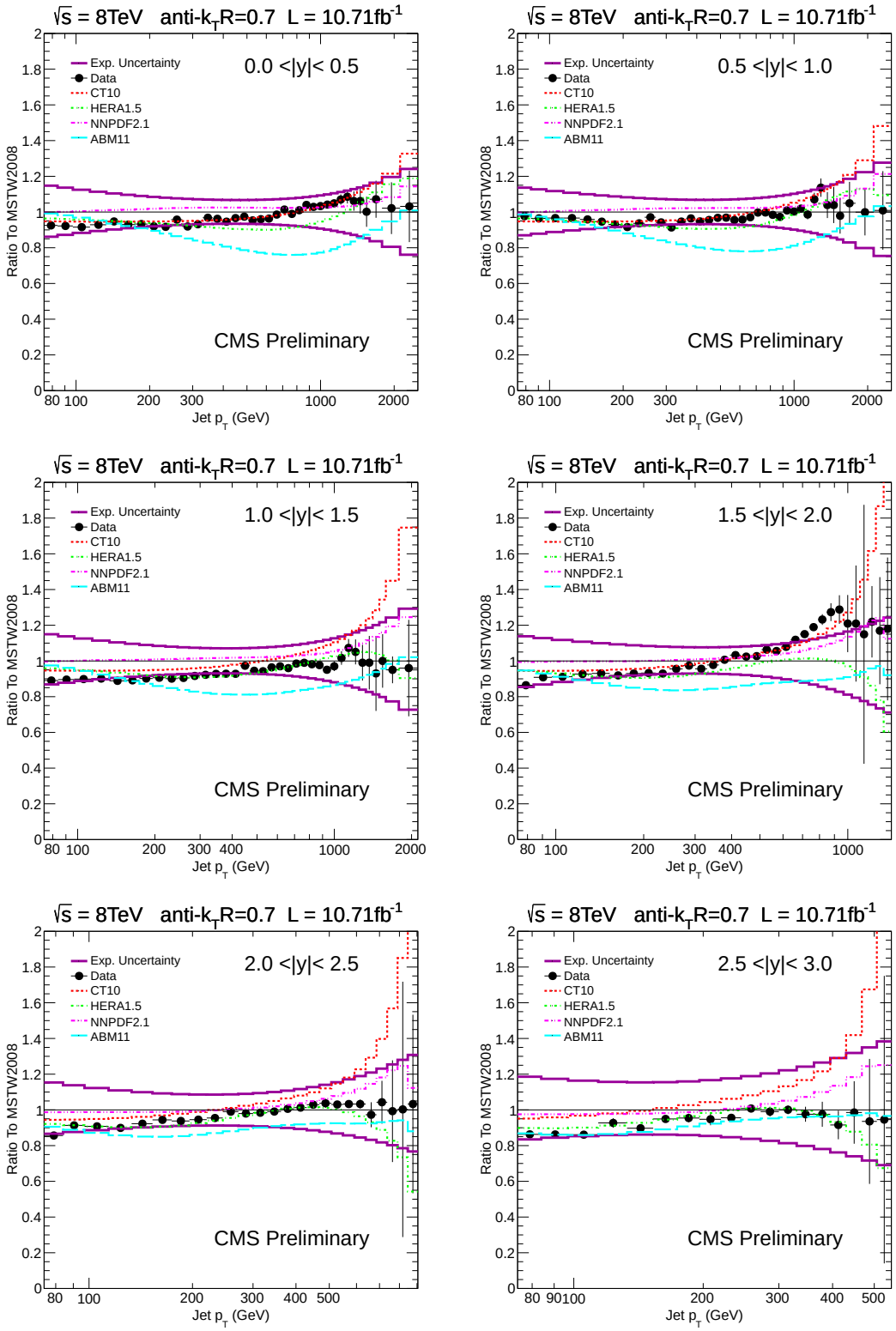

Figure 9: Ratio of data over theory at NLO times NP correction for the MSTW2008 PDF set. For comparison predictions employing four other PDF sets are shown in addition to the total experimental systematic uncertainty (band enclosed by full magenta lines). The error bars correspond to the statistical uncertainty of the data.

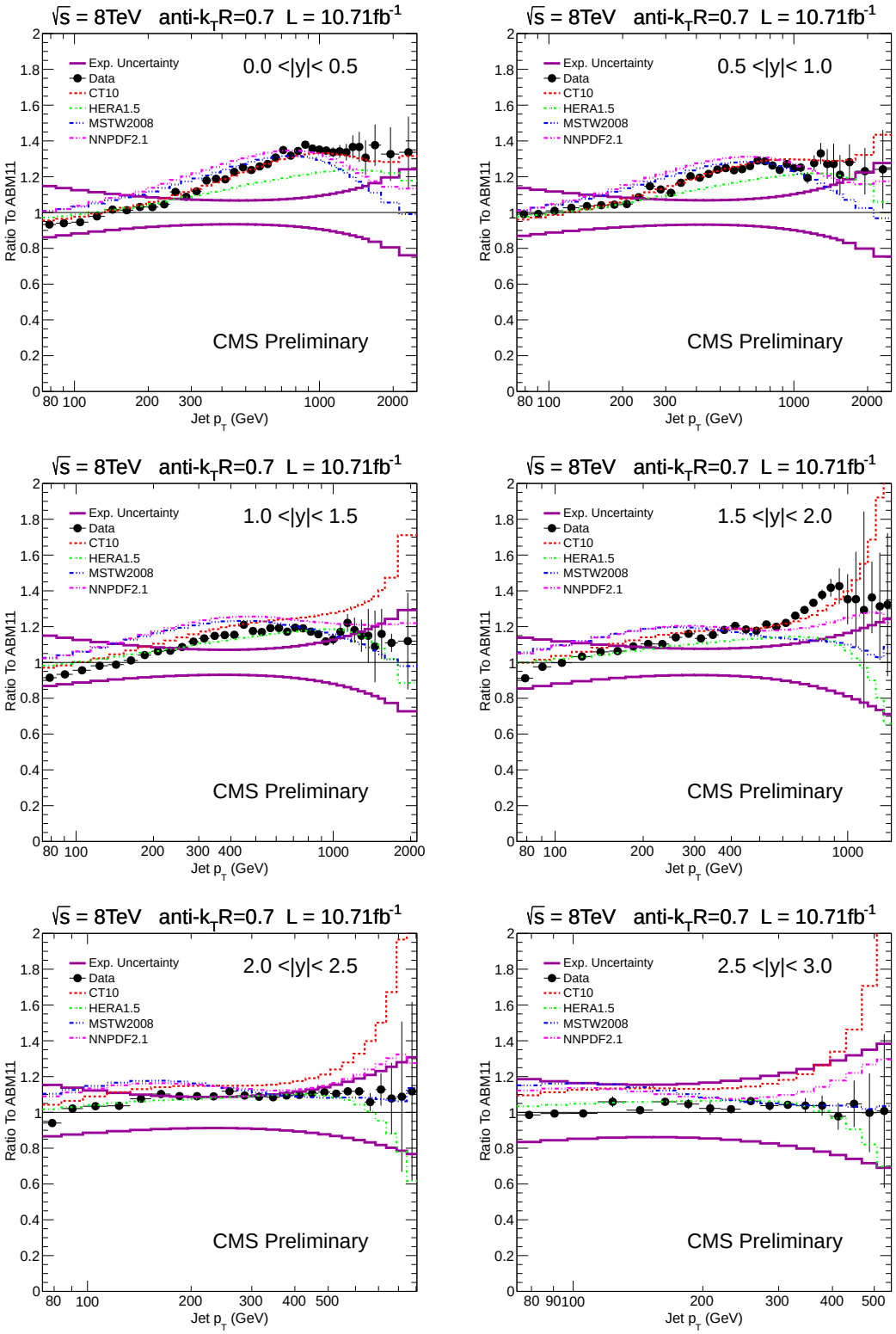

Figure 10: Ratio of data over theory at NLO times NP correction for the ABM11 PDF set. For comparison predictions employing four other PDF sets are shown in addition to the total experimental systematic uncertainty (band enclosed by full magenta lines). The error bars correspond to the statistical uncertainty of the data.

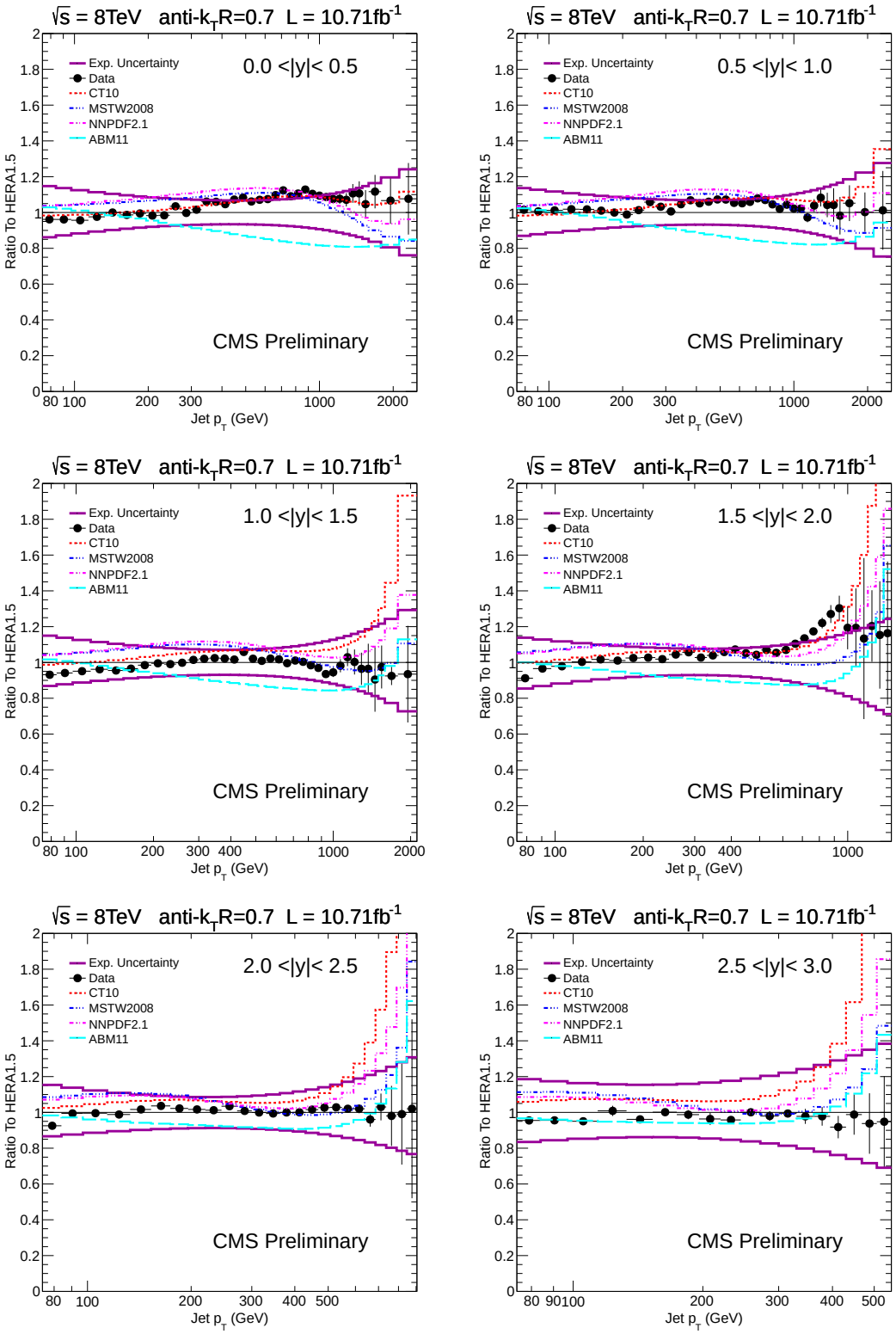

Figure 11: Ratio of data over theory at NLO times NP correction for the HERA1.5 PDF set. For comparison predictions employing four other PDF sets are shown in addition to the total experimental systematic uncertainty (band enclosed by full magenta lines). The error bars correspond to the statistical uncertainty of the data.